The Astrophysical Journal Letters, 940:L19 (12pp), 2022 November 20 https://doi.org/10.3847/2041-8213/ac990b

Detection of Intracluster Globular Clusters in the First JWST Images of the Gravitational Lens Cluster SMACS J0723.3–7327 at $z = 0.39$

Myung Gyoon Lee[1], Jang Ho Bae[1], and In Sung Jang[2]
[1] Astronomy Program, Department of Physics and Astronomy, SNUARC, Seoul National University, 1 Gwanak-ro, Gwanak-gu, Seoul 08826, Republic of Korea
mglee@astro.snu.ac.kr
[2] Department of Astronomy & Astrophysics, University of Chicago, 5640 South Ellis Avenue, Chicago, IL 60637, USA
Received 2022 August 9; revised 2022 October 3; accepted 2022 October 10; published 2022 November 21

Abstract

We present a survey of globular clusters (GCs) in the massive gravitational lens cluster SMACS J0723.3–7327 at $z = 0.39$ based on the early released JWST/NIRCam images. In the color–magnitude diagrams of the point sources, we clearly find a rich population of intracluster GCs that are spread over a wide area of the cluster. Their ages, considering the cluster redshift, are younger than 9.5 Gyr. The F200W (AB) magnitudes of these GCs, 26.5 mag $<$ F200W$_0$ $<$ 29.5 mag, correspond to -15.2 mag $< M_{\rm F200W} < -12.2$ mag, showing that they belong to the brightest GCs (including ultracompact dwarfs). The spatial distributions of these GCs show a megaparsec-scale structure elongated along the major axis of the brightest cluster galaxy. In addition, they show a large number of substructures, some of which are consistent with the substructures seen in the map of diffuse intracluster light. The GC number density map is, in general, consistent with the dark matter mass density map based on the strong lensing analysis in the literature. The radial number density profile of the GCs in the outer region is steeper than the dark matter mass profile obtained from lensing models. These results are consistent with those for the GCs found in the deep HST images of A2744, another massive cluster at $z = 0.308$, and in simulated galaxy clusters. This shows that the intracluster GCs are an excellent independent tool to probe the dark matter distribution in galaxy clusters, as well as reveal the cluster assembly history in the JWST era.

Unified Astronomy Thesaurus concepts: Early-type galaxies (429); Giant elliptical galaxies (651); Globular star clusters (656); Rich galaxy clusters (2005); Galaxy clusters (584); Intracluster medium (858)

1. Introduction

Massive galaxy clusters that show (strong and weak) gravitational lensing effects are ideal targets to investigate the large-scale distribution of dark matter and the relation between the dark matter and the baryonic matter (e.g., Lotz et al. 2017; Fox et al. 2022, and references therein). The baryonic matter in galaxy clusters is composed mainly of galaxies and the intracluster medium (ICM). The primary components in the ICM are X-ray-emitting hot gas, intracluster light (ICL), intracluster globular clusters (GCs), and intracluster planetary nebulae. Among them, the intracluster GCs are, because they are compact and abundant, very useful to study the relation between dark matter and baryonic matter at large scales.

Wide-field imaging has been a main tool for the survey of intracluster GCs in the nearby galaxy clusters (Lee et al. 2010; Peng et al. 2011; Durrell et al. 2014; Harris et al. 2017; Iodice et al. 2017; Hilker et al. 2018; Madrid et al. 2018; Harris et al. 2020). The high-resolution power of the Hubble Space Telescope (HST) enables us to probe the intracluster GCs in the more distant galaxy clusters and study the relation between the intracluster GC and dark matter distributions (Alamo-Martínez et al. 2013; Lee & Jang 2016; Alamo-Martínez & Blakeslee 2017).

Using the deep Advanced Camera for Surveys (ACS) F814W and WFC3/F105W images of the HST Frontier Fields (Lotz et al. 2017), Lee & Jang (2016) presented a survey of GCs including ultracompact dwarfs (UCDs) in the massive merging cluster A2744 (known as the Pandora cluster) at $z = 0.308$. They found a rich population of GCs and UCDs in the cluster, a significant fraction of which are intracluster GCs that are spread over a wide area of the cluster. They showed that the number density map of the intracluster GCs in A2744 is similar to the dark matter mass map derived from CATS strong lensing models (Jauzac et al. 2015).

In this study, we search for GCs of SMACS J0723.3–7327 (hereafter SMACS 0723), a massive cluster at $z = 0.39$, which is farther than A2744, using the first JWST/NIRCam images released on 2022 July 12 as part of the early release JWST images (Pontoppidan et al. 2022; Rigby et al. 2022). Recently, Mowla et al. (2022) found five GCs that are considered to be associated with the Sparkler galaxy at $z = 1.38$, which is gravitationally lensed by SMACS 0723 from the JWST/NIRCam and HST/ACS images. Our primary goal is to find and study the GCs that belong to SMACS 0723. The basic properties of SMACS 0723 are listed in Table 1.

The HST observations of this cluster were included in the HST Snapshot survey (Repp & Ebeling 2018) and the RELICS program (Coe et al. 2019), providing the magnitudes of the brightest cluster galaxy (BCG), F814W = 19.14 ($M_{\rm F814W} = -22.9$) mag and F606W = 20.35 ($M_{\rm F606W} = -22.0$) mag. We first checked the HST data of SMACS 0723 available in the archive but found that the images are too shallow to detect GCs in this cluster. The JWST/NIRCam data go much deeper for these GCs that are composed of old stars, enabling us to detect them. Object SMACS 0723 shows a large number of gravitationally lensed images of background sources, which were used for tracing dark matter in the cluster (Caminha et al. 2022; Golubchik et al. 2022; Mahler et al. 2022; Pascale et al. 2022). The mass of SMACS 0723 based on strong lensing models is $M(R < 400\ {\rm kpc}) \sim 3 \times 10^{14}\ M_{\odot}$ (Mahler et al. 2022), and the mass

Table 1
Basic Properties of SMACS 0723

Parameter	Value	References
Heliocentric velocity	116,919 km s^{-1}	1, 2
Redshift	$z = 0.39$	1, 2
Luminosity distance[a]	2170 Mpc	1
Distance modulus[a]	$(m - M)_0 = 41.69 \pm 0.15$	1
Image scale[a]	5.453 kpc $arcsec^{-1}$ = 327.16 kpc $arcmin^{-1}$	1
Age at redshift[a]	9.474 Gyr	1
Foreground extinction	$A_V = 0.585$, $A_I = 0.328$	3
	$A_{F090W} = 0.296$, $A_{F150W} = 0.134$, $A_{F200W} = 0.083$	3
	$A_{F277W} = 0.053$, $A_{F356W} = 0.039$, $A_{F444W} = 0.031$	3
Velocity dispersion	$\sigma_v = 1, 180 \pm 170$ km s^{-1}	2
Mass	$M(R < 400$ kpc$) = 3 \times 10^{14}\ M_\odot$	2 (lensing)
	$M(R < 1$ Mpc$) = 8 \times 10^{14}\ M_\odot$	4 (Planck)

Note.
[a] NED values for $H_0 = 67.8$ km s^{-1} Mpc^{-1}, $\Omega_M = 0.308$, $\Omega_\Lambda = 0.692$.
References. (1) The NASA/IPAC Extragalactic Database (NED); (2) Mahler et al. (2022); (3) Schlegel et al. (1998); (4) Pascale et al. (2022).

derived from Planck observations is $M(\text{Planck}) = 8.39 \times 10^{14}\ M_\odot$ (Pascale et al. 2022). Mahler et al. (2022) presented a mean redshift of 26 cluster members located in the central region of SMACS 0723, $z = 0.3877$, which is slightly smaller than the redshift of the BCG, $z = 0.3912$. In the following analysis, we adopt $z = 0.39$ and the position of the BCG as the cluster center. We adopt the cosmological parameters $H_0 = 67.8$ km s^{-1} Mpc^{-1}, $\Omega_\Lambda = 0.7$, and $\Omega_\Lambda = 0.3$. At the adopted distance of SMACS 0723 ($d_L = 2170$ Mpc, $(m - M)_0 = 41.69$), 1″ (1') corresponds to 5.453 (327.16) kpc.

This paper is organized as follows. The data and data reduction are described in Section 2 and 3, and the main results are given in Section 4. The main results are discussed in Section 5 and summarized in the final section.

2. Data

In the data set of the first released JWST images of SMACS 0723, we use NIRCam images obtained with three short-wavelength (SW) filters (F090W, F150W, and F200W) and three long-wavelength (LW) filters (F277W, F356W, and F444W) on 2022 June 7 (see the field locations in Figure 1 of Pontoppidan et al. 2022). The total exposure time is 7537 s for each filter. The SW filter images have an image scale of 0.″03 $pixel^{-1}$, and the LW images have a twice as large image scale of 0.″06 $pixel^{-1}$.

The released images include two fields: a cluster central field that covers the central region of the cluster and a parallel field that covers the outskirts of the cluster, as shown in Figure 1(a). The field of view for each of the NIRCam images is 129″ × 129″, and the gap between the central and parallel fields is 44″. The parallel field is ∼2.′9 to the southwest of the central field. The radial coverage of the parallel field is 550 kpc $< R <$ 1.3 Mpc, where R is the projected radial distance from the cluster center. In Figure 1(a), we display gray-scale maps of F200W images of the two fields. We mark the brightest galaxies (G2, G3, G4, and G5) including the BCG in the central field. The edge regions of each field marked in burgundy have low signal-to-noise ratios in the combined images, so they are not used for the final analysis. In Figures 1(b)–(e), we also display the zoomed-in color image of the central field showing the BCG region and the zoomed-in images of the BCG region that clearly show GCs, which will be described in the following.

3. Data Reduction

We use F200W images, which have the highest sensitivity among the six NIRCam images, as a reference image for point-source detection.[3] We adopt the AB magnitudes in this study. The relations between the AB and Vega magnitudes in the JWST CRDS[4] are mag(AB) − mag(Vega) = 0.504, 1.243, 1.706, 2.315, 2.824, and 3.242 for F090W, F150W, F200W, F277W, F365W, and F444W.

The mean effective radii of typical GCs in the Milky Way are about 3 pc, and the FWHM values of the point sources in the JWST/NIRCam/SW images are about 2.4 pixels (0.″072 = 0.39 kpc). Thus, typical GCs appear as point sources in the JWST/NIRCam images of SMACS 0723 (see also Faisst et al. 2022). We select the point sources from which GCs are segregated as follows.

3.1. Photometry of the Extended Sources

First, we obtain the photometry of the sources (including both extended and point sources) detected with a 10σ threshold in the images using SExtractor (Bertin & Arnouts 1996). We carry out dual-mode photometry with the F277W image as a reference image for source detection. As the pixel scales for the LW and SW detectors are different, the SW images were reprojected and aligned with respect to the F277W image using the wregister task in IRAF (Tody 1986; Science Software Branch at STScI 2012) and astroalign (Beroiz et al. 2020), respectively. For aligning the images, we use the positions of several stars. We use LW images for the analysis of galaxies because the normal red sequence of galaxies in galaxy clusters is better distinguishable in the LW color–magnitude diagrams (CMDs) than in the SW CMDs, as shown in the following.

Figure 2 displays an effective radius r_h versus F277W (AUTO) magnitudes of the sources detected with SExtractor. We also mark the sources with small stellarity < 0.4 (red squares) and large stellarity > 0.8 (blue squares). The prominent narrow slanted sequence dominated by blue squares represents the point sources with small effective radii. Some of the bright sources with large effective radii are found to have a large value of stellarity > 0.8, so we consider that effective radius is a better indicator to

[3] JWST user documentation, https://jwst-docs.stsci.edu.
[4] https://jwst-crds.stsci.edu

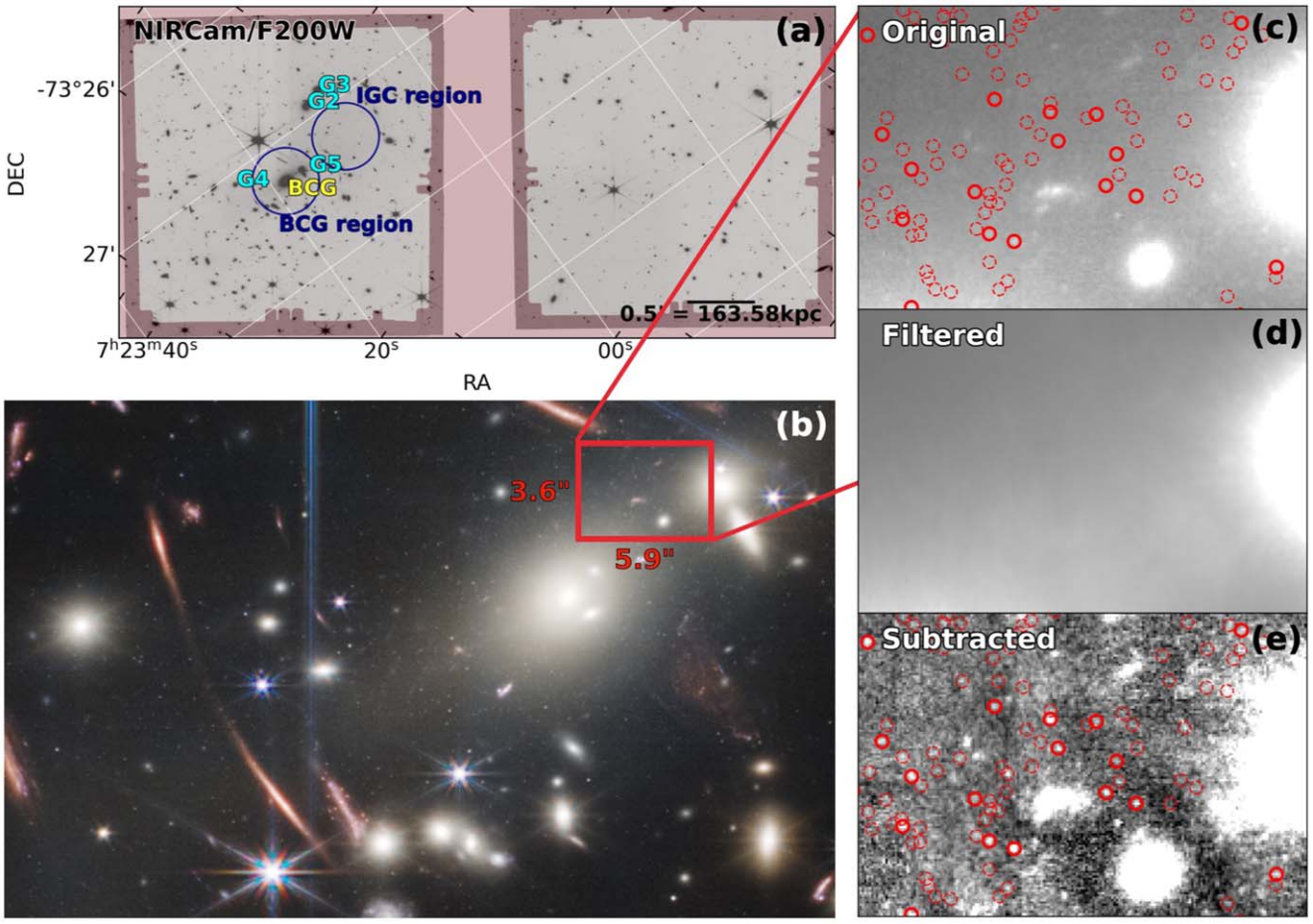

Figure 1. (a) Gray scale maps of the F200W images of the central (left) and parallel (right) fields of SMACS 0723 (see also Figure 1 of Pontoppidan et al. 2022). Two large circles with radius of 15″ represent the BCG region and intracluster GC region, and the brightest galaxies including the BCG are labeled. Burgundy color denotes the edge regions with low signal to noise ratios in the combined images, which were not used for analysis. (b) A zoomed-in view of the BCG region in the central field of SMACS 0723: the Sparkler galaxy ($z = 1.38$, with a red linear shape embedding several red point sources) is at 15″ east of the BCG. (c, d, and e) Zoomed-in views of the original F200W image of the red box region in (b), the same image smoothed with a ring median filter, and the background-subtracted image. Red circles represent the point sources (thin dotted line) and GC candidates (thick solid line) found in this study, which are visible more clearly in the background-subtracted image.

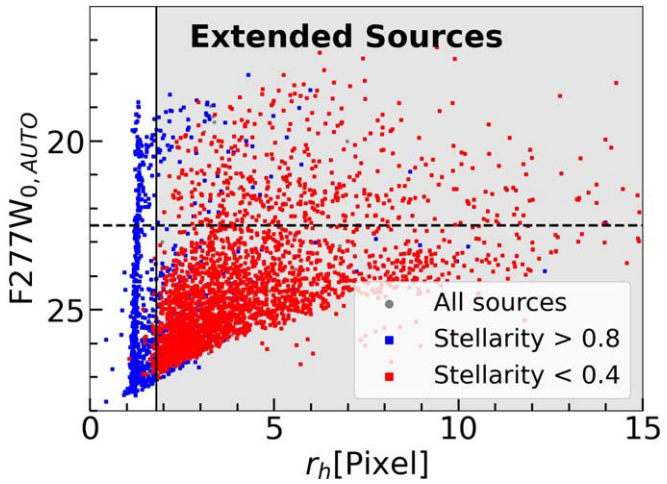

Figure 2. Effective radius r_h vs. F277W (AUTO) magnitudes of the sources detected with SExtractor. Red squares represent the sources with stellarity <0.4, and blue squares denote the sources with stellarity > 0.8. The narrow slanted line dominated by the blue squares represents the point sources. Note that some bright sources ($F277W_0 < 22.5$ mag) with stellarity >0.8 have large effective radii, $r_h > 1.8$ pixels. In this study, we select extended sources using the effective radius criterion, $r_h > 1.8$ pixels in the F277W image, as marked by the vertical black line.

distinguish extended sources than stellarity. In this study, we select extended sources using the effective radius criterion: $r_h > 1.8$ pixels in the F277W image.

The extended sources include galaxies and gravitationally lensed sources. We adopt AUTO magnitudes for the extended sources provided by SExtractor and use them for the analysis of photometric properties of the galaxies in the following. We calibrate the instrumental magnitudes from SExtractor using the JWST source catalog.

3.2. Photometry of the Point Sources

For better detection of the point sources in the images that include a number of bright galaxies, we subtract the diffuse background light from the original images. First, we derive a smooth background image of the original F200W image using a ring median filter with $r_{in} = 18$ and $r_{out} = 20$ pixels. Then we subtract this smooth background image from the original image and use the background-subtracted image for the point-source detection.

3.2.1. Point-spread Function Fitting Photometry

We obtain the point-spread function (PSF) fitting photometry of the sources in the F150W and F200W images of the central and

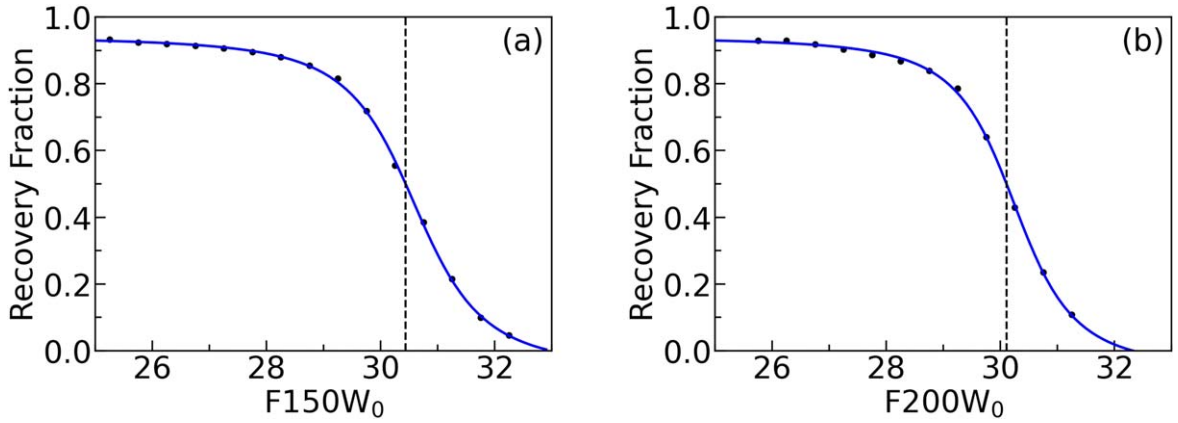

Figure 3. Completeness (recovery fraction) vs. F150W (a) and F200W (b) magnitudes of the point sources. Blue solid lines denote the fitting results. The vertical black lines mark 50% completeness limits: $F150W_{0,lim} = 30.44$ and $F200W_{0,lim} = 30.11$ mag.

parallel fields using DAOPHOT (Stetson 1987). We derive the PSF using the isolated bright stars in the images. Among the detected sources, we select the point sources using the sharpness parameter and photometric errors provided by DAOPHOT.

We calibrate the instrumental PSF-fitting magnitudes using the total magnitudes of bright stars given in the source catalog of SMACS 0723 included in the released data. We use only the bright stars 21 mag $< F150W_0$, $F200W_0 < 24$ mag, which have small errors. However, it is noted that this zero-point calibration is preliminary. There could be a substantial (systematic) error associated with the preflight version of the JWST catalog (Boyer et al. 2022). The catalog of the point-source photometry in this study will be publicly available at GitHub.[5]

We calculate the extinction values for the JWST filters from the extinction value for the V band given by Schlegel et al. (1998) and Schlafly & Finkbeiner (2011) using the extinction law (Fitzpatrick 1999; Indebetouw et al. 2005) and the filter information in the SVO filter profile service website (Rodrigo et al. 2012; Rodrigo & Solano 2020). The extinction values are listed in Table 1. We apply the foreground extinction correction to the apparent magnitudes and use the subscript 0 for the foreground extinction–corrected magnitudes.

3.2.2. Completeness Tests

We estimate the photometric completeness of the point sources using the artificial star experiments with DAOPHOT/ADDSTAR. We added 2500 artificial stars with a range of magnitude and color to each of the F150W and F200W images. We repeat this process 400 times for each set of images so that the total number of added artificial stars in each band is 1 million. We obtain the photometry of these sources using the same procedure as used for the original images. Then we select the recovered/added stars with the GC color range and estimate the completeness from the number ratio of the recovered stars to the added stars as a function of magnitude. Figure 3 displays the completeness versus magnitude for the F150W and F200W bands. We fit the data using the interpolation function given in Harris et al. (2009), $f(m) = 0.5(\beta - \alpha(m - m_0)/\sqrt{1 + \alpha^2(m - m_0)^2})$, where β is the maximum completeness, m_0 is the magnitude for $\beta/2$, and α represents the slope around m_0, as shown by the solid lines in the figure. The limiting magnitudes for 50% photometric completeness are $F150W_0 = 30.44$ and $F200W_0 = 30.11$ mag. The artificial stars are also used to correct the completeness of the radial number density profile, which is shown in Figure 9.

[5] https://github.com/hanlbomi/SMACS-J0723.3-7327-GCs

4. Results

4.1. CMDs of the Galaxies

In Figure 4, we display the LW (F277W versus (F277W – F356W)) and SW (F200W versus (F150W – F200W); in AUTO magnitudes) CMDs of the extended sources in the central field of SMACS 0723. We also mark the cluster member galaxies ($N = 26$) confirmed with spectroscopic observations (Mahler et al. 2022), the selected bright galaxies (including the BCG), and the known gravitational lens image sources in Mahler et al. (2022).

IIn the F277W versus (F277W – F356W) CMD, two prominent features are noted: an LW-blue vertical sequence with $(F277W - F356W)_0 \approx -0.6$ and an LW-red slanted sequence with $(F277W - F356W)_0 \approx +0.1$. The known cluster members are mostly located in the bright part of the LW-blue sequence. The known cluster members are mostly early-type galaxies, showing that this sequence corresponds to the normal red sequence in the optical CMDs of galaxy clusters. So these member galaxies were plotted with red circles. The selected bright galaxies including the BCG are also located in the bright part of this sequence. The presence of a large number of galaxies located in this LW-blue sequence shows that SMACS 0723 is indeed a rich cluster.

IIn contrast, the known gravitational lens image sources are mostly located along the LW-red sequence but with a larger scatter than the LW-blue sequence. They look red in the released color images based on the combination of all SW and LW filter images. The gravitational lens image sources have much higher redshifts than that of SMACS 0723, so they are not the cluster members. They are background galaxies, most of which show some star formation activity (i.e., late-type galaxies having different colors compared with early-type galaxies).

However, the F200W versus (F150W – F200W) CMD shows only one notable slanted sequence at $(F150W - F200W)_0 \approx +0.2$. Both the cluster member galaxies and the lens image sources are located mostly in the same sequence, so they are hardly distinguished in this sequence.

Therefore, as the red-sequence galaxies are mostly early-type cluster members, we select those located along the LW-blue sequence as marked in the LW CMD: $-0.65 < (F277W - F356W)_0 < -0.45$. We use them to check any correlation between the GCs and the galaxies in the following analysis.

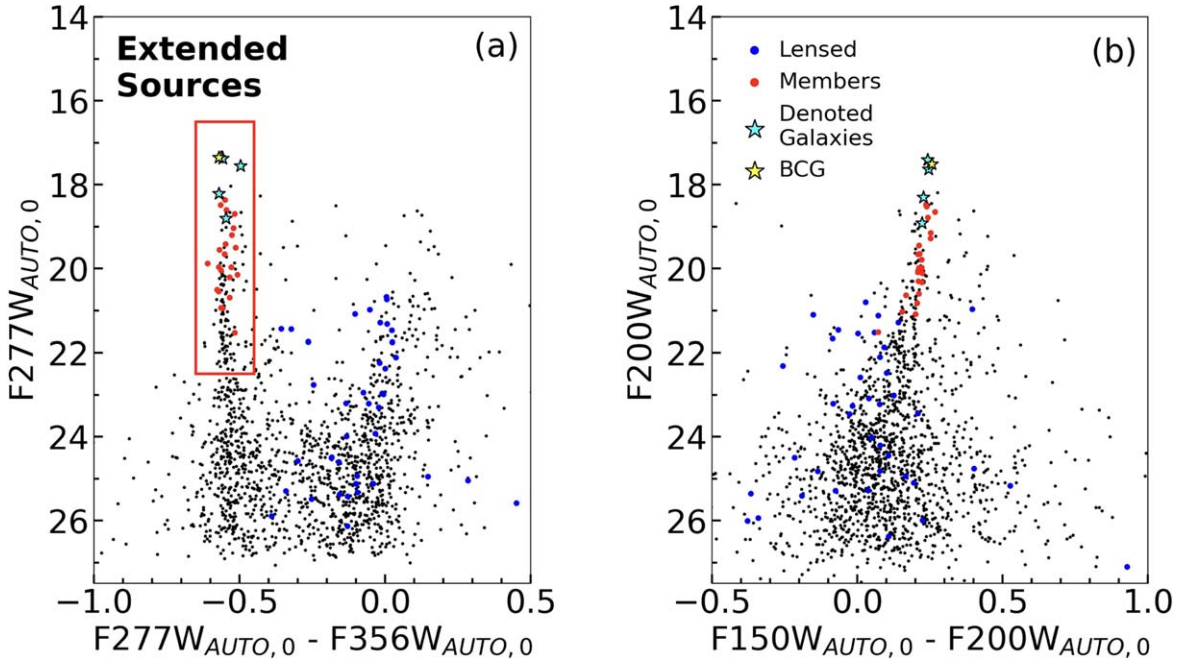

Figure 4. The LW (F277W vs. (F277W – F356W)) and SW (F200W vs. (F150W – F200W)) CMDs of the extended sources with AUTO magnitudes in the central field of SMACS 0723. Red circles denote the spectroscopically confirmed cluster member galaxies, and blue circles represent the gravitational lens image sources (Mahler et al. 2022). The yellow star is the BCG, and cyan stars represent the bright galaxies (G2, G3, G4, and G5) marked in Figure 1. The red box in the left panel represents the selection criteria for the optically red sequence galaxies, which are mostly early-type members of the cluster. Note that the blue member galaxies in (F277W – F356W) colors are optically red galaxies, so they are plotted with red circles.

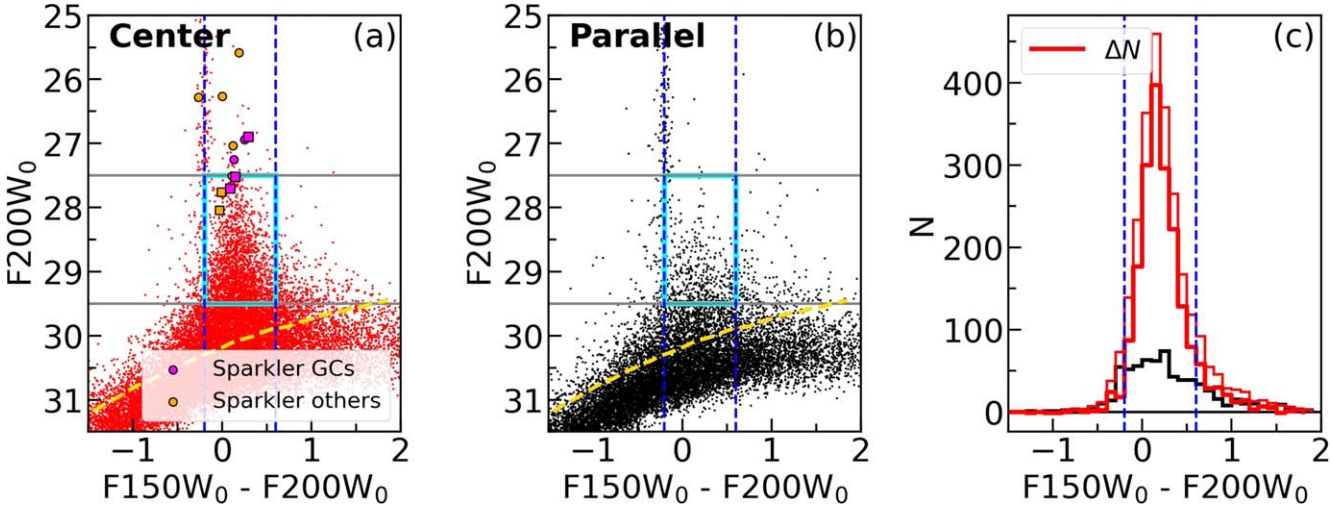

Figure 5. The F200W vs. (F150W – F200W) CMDs of the point sources in the central (a) and parallel (b) fields of SMACS 0723. Magenta and orange circles, respectively, represent the GCs and other compact sources of the Sparkler galaxy ($z = 1.38$) in Mowla et al. (2022). Magenta and orange boxes are the point sources selected in this study. The sources inside the cyan box of the central field are mostly GCs belonging to SMACS 0723. Cyan boxes represent the boundary for selecting the GC candidates in this study. The yellow dashed lines mark the 50% completeness limit. In panel (c), the thick red line denotes the net color histogram of the point sources with 27.5 mag $<$ F200$_0$ $<$ 29.5 mag in the central field (thin red line) after subtracting the contribution of the background based on the parallel field (black line).

4.2. CMDs of the Point Sources: Detection of the GCs

Figure 5 displays F200W versus (F150W – F200W) CMDs of the point sources in the central and parallel fields. The CMD of the central field clearly shows a strong concentration of the point sources with GC colors ($-0.2 <$ (F150W $-$ F200W)$_0 <$ 0.6) in the magnitude range of 26.5 mag $<$ F200W$_0 <$ 30 mag. In contrast, a much smaller number of sources are located in the same region of the CMD of the parallel field. This indicates that most of these sources in the central field belong to SMACS 0723.

We also plot the GCs and other compact source candidates in the image 2 field of the Sparkler galaxy ($z = 1.38$) located at $R = 15''$ (82 kpc) east of the BCG in Mowla et al. (2022). We cross-matched the compact sources in Mowla et al. (2022) with our photometry and found that all of the sources ($N = 12$) were successfully recovered. However, only five of them passed our point-source selection criteria. This indicates that a significant fraction of the compact sources in Mowla et al. (2022) are at least marginally resolved or do not follow the clean JWST/NIRCam PSFs. These sources are located in the similar GC

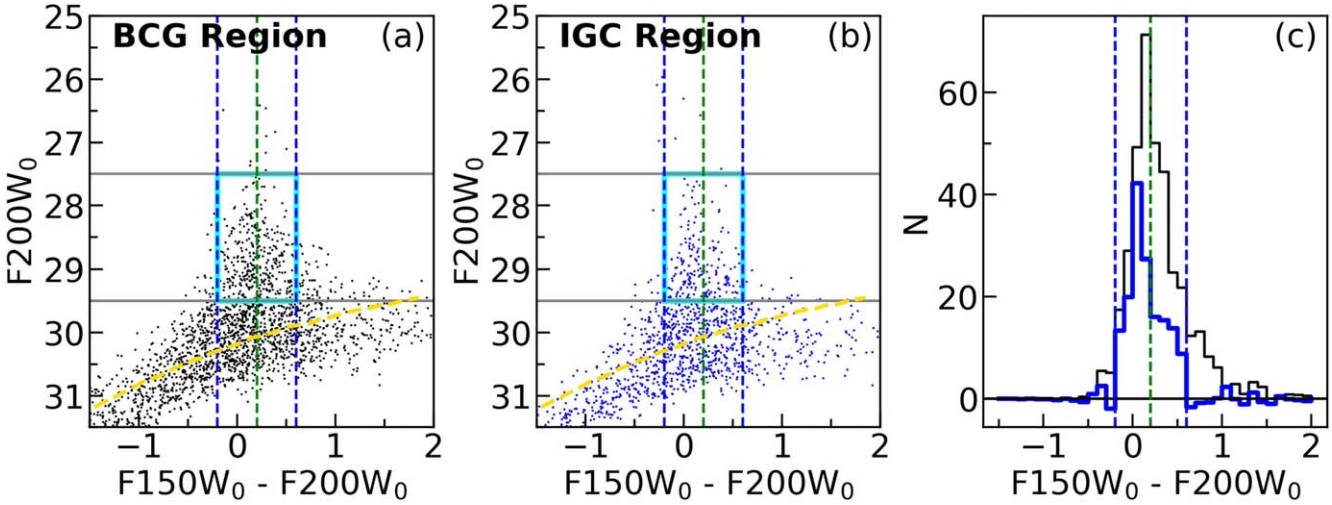

Figure 6. (a) and (b) F200W vs. (F150W – F200W) CMDs of the point sources in the BCG and intracluster GC regions in the central field of SMACS 0723, as marked in Figure 1. The yellow dashed lines mark the 50% completeness limit. (c) Color histograms of the BCG (black line) and intracluster GC (blue line) regions after subtracting the contribution of the background based on the parallel field. Note that the color distribution of the intracluster GC region shows a strong peak at $(F150W - F200W)_0 = 0.05$, while that of the BCG region shows a strong peak at 0.1 redder color, $(F150W - F200W)_0 = 0.15$. Note also that both regions show a broad color distribution across the peak. Cyan boxes represent the boundary for selecting GC candidates, and green dashed lines mark the boundary for separating blue and red GCs.

color range, and the matched GCs occupy the brightest part of the GCs (27 mag $< F200W_0 <$ 28 mag). Note that there are dozens more sources in the similar CMD region (26.5 mag $< F200W_0 <$ 28 mag) of the central field, but few are in the CMD of the parallel field. They are probably UCDs, but some of them may be candidates for background GCs that were gravitationally lensed like the Sparkler galaxy GCs. The brightest of them are as bright as $F200W_0 \approx 26.5$ mag.

In Figure 5, we also plot the color histograms of the point sources with 27.5 mag $< F200W_0 <$ 29.5 mag in the central (thin red line) and parallel (thick black line) fields. Assuming the parallel field as the background, we subtract the contribution of the background from the color histogram of the central field. The resulting net color histogram of the central field (thick red line) shows a significant excess component that is close to Gaussian with a peak at $(F150W - F200W)_0 \approx 0.2$. This indicates that these point sources are mostly genuine GCs that belong to SMACS 0723.

We select the GC candidate sample using the cyan box marked in the figure ($-0.2 < (F150W - F200W)_0 < +0.6$ and 27.5 mag $< F200W_0 <$ 29.5 mag) for the following analysis. We conservatively selected the GC candidates with photometric completeness higher than 70% ($F200W_0 <$ 29.5 mag). The number of selected GC candidates in the two fields is about 2500. Figures 1(c)–(e) display the zoomed-in images of the sample section of the BCG region that show these GCs better after subtracting the smooth background image from the original image.

The apparent magnitude range (27.5 mag $< F200W_0 <$ 29.5 mag) of these sources at the cluster distance corresponds to the absolute magnitude range of -14.2 mag $< M_{F200W} < -12.2$ mag, so these GCs belong to the bright end of the GCs, which includes the UCDs. Considering the redshift of SMACS 0723, the ages of these GCs are younger than 9.5 Gyr. The ages of most Milky Way GCs range from 11 to 13 Gyr, with a mean value of 12.3 ± 0.4 Gyr (Oliveira et al. 2020; Kang & Lee 2021). Thus, the SMACS 0723 GCs may be about 8 Gyr old, assuming that they formed as the Milky Way GCs.

We select two representative regions to check any difference between galaxy and intracluster GCs: the BCG region (at $R < 15''$ from the BCG center) and the intracluster GC region (with a radius of $15''$) that covers the western loop (Mahler et al. 2022; Montes & Trujillo 2022; Pascale et al. 2022) and no bright galaxies, as marked in Figure 1(a). In Figures 6(a) and (b), we display F200W versus (F150W – F200W) CMDs of the point sources in the BCG region and the intracluster GC region. We also plot the color histograms of both regions in Figure 6(c). We derived the color histograms for the BCG and intracluster GC regions after subtracting the background contribution based on the parallel field. Note that the color distribution of the intracluster GC region shows a strong peak at $(F150W - F200W)_0 = 0.05$ and a weaker component at $(F150W - 200W)_0 \approx 0.4$. In contrast, the color distribution of the BCG region shows a strong peak at $(F150W - F200W)_0 = 0.15$, which is 0.1 redder than the peak in the intracluster GC region. We calculate the blue GC fractions, obtaining $f(\text{blue GC}) = 65\%$ for the intracluster GC region and 54% for the BCG region. Thus, the intracluster region has a higher fraction of blue GCs than the BCG region. The color distribution for the intracluster GC region is broad across the peak color, showing that there are not only blue GCs but also red GCs, although the blue GC fraction is higher. The presence of both subpopulations in this region implies that the origin of the intracluster GCs is dual; the dominant progenitors of the intracluster GCs are low-mass dwarf galaxies, and the minor progenitors are massive galaxies, as discussed in the case of Virgo intracluster GCs by Lee et al. (2010).

Considering these, we divide the GCs in the entire field into two subpopulations according to their colors: the blue (metal-poor) GCs with $-0.2 < (F150W - F200W)_0 < +0.2$ and the red (metal-rich) GCs with $+0.2 < (F150W - F200W)_0 < +0.6$. We use these blue and red GCs for the following analysis to study any difference between the two subpopulations.

4.3. Spatial Distributions of the GCs

Figure 7(a) shows the spatial distribution of the GC candidates selected in the central field. In Figure 7(b), we plot the number density contours and color gradient map of these

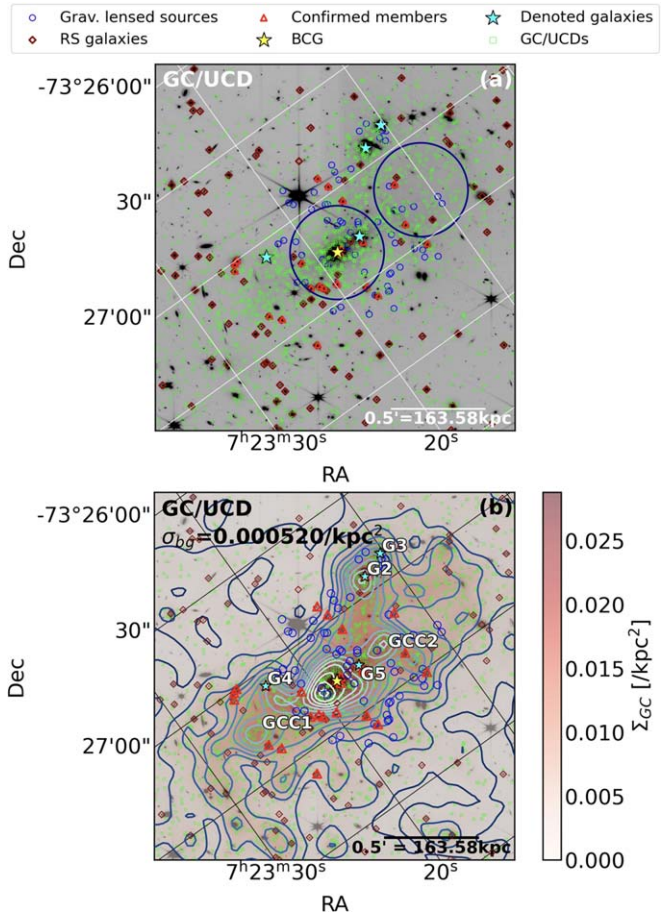

Figure 7. (a) Spatial distribution of the GCs (green squares) in the gray-scale map of the F200W image for the central field of SMACS 0723. Red triangles represent the confirmed cluster member galaxies, and dark red diamonds denote the selected bright red-sequence galaxies (with $-0.65 < (\mathrm{F277W} - \mathrm{F356W})_0 < -0.45$ and $\mathrm{F277W}_0 < 22.5$ mag). Blue open circles represent the gravitational lens image sources (Mahler et al. 2022). Yellow and cyan stars denote the BCG and other bright galaxies. Two large circles mark the BCG and intracluster GC regions. (b) Contour map and color gradient map of the GC number density in the gray-scale map of the F200W image. The contours were plotted from the $2\sigma_{\mathrm{bg}}$ level with $4\sigma_{\mathrm{bg}}$ steps. The color-scale bar represents the GC number density per square kiloparsec, and GCC 1 and GCC 2 denote GC clumps.

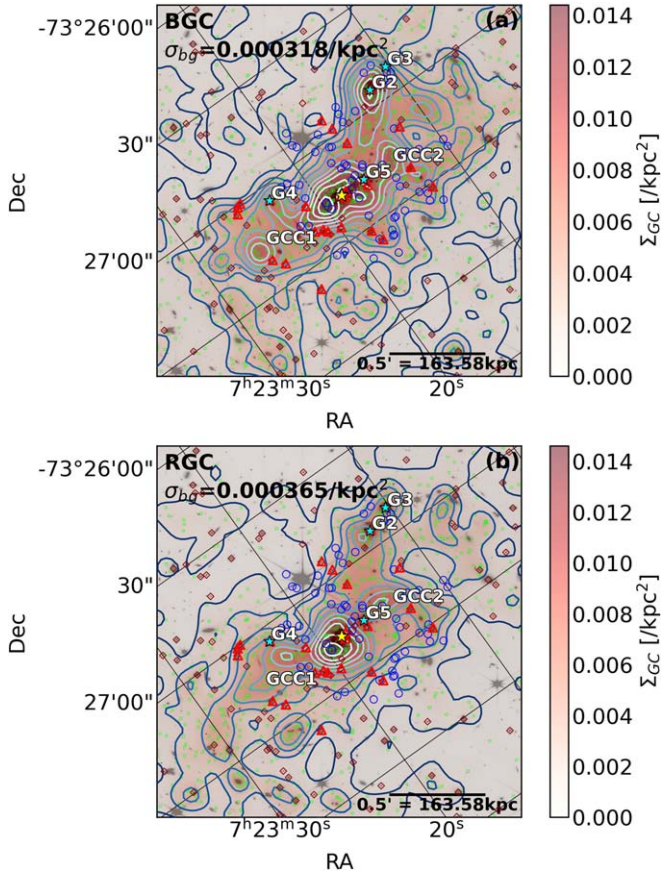

Figure 8. Same as Figure 7(b) but for blue ($-0.2 < (\mathrm{F150W} - \mathrm{F200W})_0 < 0.2$) and red ($0.2 < (\mathrm{F150W–F200W})_0 < 0.6$) GCs.

sources on the gray-scale map of the F200W image. The contours were smoothed with a Gaussian smoothing scale, $\sigma_{\mathrm{G}} \simeq 3''$. The lowest level in the contours starts with $2\sigma_{\mathrm{bg}}$, where σ_{bg} is estimated from the background fluctuation of the selected GC candidates in the low-density region of the parallel field: $\sigma_{\mathrm{bg}} = 0.000520 \pm 0.000029$ kpc^{-2}. The step between contours is $4\sigma_{\mathrm{bg}}$. We also mark the locations of the known cluster members, the selected brightest galaxies (including the BCG), the gravitational lens image sources (Mahler et al. 2022), and the red-sequence galaxies selected in this study to check any spatial correlation with the GCs.

Several features are noted in this figure. First, the overall distribution of the GC candidates clearly shows a central concentration around the BCG that is located close to the galaxy cluster center. This implies that most of the selected GC candidates are indeed members of SMACS 0723. The strongest peak of the GC number density is slightly offset to the east of the BCG center, and this can be explained as follows. There are two galaxies close to the BCG center in the west, so it is difficult to completely subtract the stellar light of these galaxies in the central region. This decreases the detection rate of the GCs in that region, causing the slight offset from the BCG center. However, the center of the contours at $R > 10''$ is consistent with the BCG center.

Second, the overall distribution of the GCs is elongated along the major axis of the BCG. Third, the spatial distribution of the GCs is much more extended than that of the stellar light of the BCG.

Fourth, strong peaks are found at the positions of some brightest galaxies. The second-strongest peak of the GC number density is seen at the position of G2, a bright elliptical member galaxy ($z = 0.3841$) at $R \approx 190$ kpc in the northwest of the BCG. Another weaker peak is seen at the position of G3, a bright galaxy close to G2. A recognizable clumping of GCs is also seen at the position of G4, another elliptical member galaxy ($z = 0.3845$). There is an isolated weak GC clump at $R \approx 300$ kpc south of the BCG, at the center of which one bright red-sequence galaxy is located. The rest of the known cluster member galaxies do not show any strong clumps of GCs.

Fifth, there is a strong concentration of GCs at $R \approx 200$ kpc in the east of the BCG (called GC clump 1, GCC 1). Interestingly, there are no recognizable bright galaxies that can be a host of these GCs. Similarly, there is a weak concentration of GCs at $R \approx 100$ kpc in the west of the BCG (called GC clump 2, GCC 2). There are no recognizable bright galaxies that can be a host of these GCs.

Sixth, there is a concentration of GCs extended to the southwest from the second-strongest G2 peak. This can be a

Table 2
Fitting Results of the GC Radial Number Density Profiles

GC Sample	BCG Component[a]	Intracluster GC Component[a]	Power-law Slope[b]
All GC	$R_{\rm eff,1} = 28.5 \pm 3.2$ kpc, $n_1 = 0.1 \pm 0.1$	$R_{\rm eff,2} = 224.5 \pm 22.1$ kpc, $n_2 = 1.3 \pm 0.3$	$\alpha = -2.0 \pm 0.2$
Blue GC	$R_{\rm eff,1} = 29.3 \pm 7.0$ kpc, $n_1 = 0.1 \pm 0.2$	$R_{\rm eff,2} = 238.9 \pm 29.1$ kpc, $n_2 = 1.3 \pm 0.3$	$\alpha = -2.1 \pm 0.2$
RGC GC	$R_{\rm eff,1} = 26.7 \pm 3.4$ kpc, $n_1 = 0.1 \pm 0.1$	$R_{\rm eff,2} = 241.7 \pm 48.6$ kpc, $n_2 = 1.5 \pm 0.6$	$\alpha = -1.9 \pm 0.3$

Notes.
[a] Fitting with the two-component Sérsic law (the BCG component plus the intracluster GC component): $\Sigma_{\rm GC}(R) = \Sigma_{\rm eff} \exp\{-b_n[(R/R_{\rm eff})^{1/n} - 1]\}$ and $b_n = 2n - 0.3271$ (Sérsic 1963; Graham & Driver 2005).
[b] Fitting with the power law for the outer region (158 kpc $< R <$ 631 kpc) of the intracluster GC component: $\Sigma_{\rm GC}(R) \propto R^{\alpha}$.

part of the large western loop-like structure, which will be described in detail later. We selected the intracluster GC region to cover this substructure, as marked by the large circle in the figure.

Finally, the GCs located outside the few bright red-sequence galaxies (including the BCG) are considered to be mostly intracluster GCs.

In Figure 8, we display the spatial distributions of the blue and red GC candidates selected in the central field. This figure shows that the central concentration of the red GCs around the BCG is more prominent than that of the blue GCs, which will also be shown by their radial number density profiles in the following. In addition, these maps show a loop-like structure with a radius of 100 kpc at $R \approx 200$ kpc west of the BCG. The structure is better seen in the red GC map. This will be compared with the substructure in the ICL map in the following.

4.4. Radial Number Density Profiles of the GCs

Adopting the BCG center as the cluster center, we derive the radial number density profile of the GCs, displaying it in Figure 9(a) after completeness correction. The number density profiles of the GCs derived before background subtraction show a flattening at $R > 90''$ in the parallel field. We estimate the background level from the sources at $R > 90''$ in the parallel field, obtaining $\Sigma_{\rm bg} = 0.000831 \pm 0.000075$ kpc^{-2}. In the figure, the number density of the GCs deceases as the clustercentric distance increases, confirming again that these GCs mostly belong to the galaxy cluster. The radial number density of the GCs keeps decreasing until $R \approx 600$ kpc. The central excess component represents the BCG GCs, while the outer part is dominated by the intracluster GCs.

In Figure 9(b), we also plot the radial number density profiles of the blue and red GCs after completeness correction. The radial profile of the red GCs shows a stronger excess in the central region than the blue GCs, and it shows an opposite trend in the outer region.

We fit the radial number density profiles of the GCs with the two-component Sérsic law (the BCG component plus the intracluster GC component): $\Sigma_{\rm GC}(R) = \Sigma_{\rm eff} \exp\{-b_n[(R/R_{\rm eff})^{1/n} - 1]\}$ and ($b_n = 2n - 0.3271$) (Sérsic 1963; Graham & Driver 2005). We also fit the data with the power law for the outer region of the intracluster GC component (158 kpc $< R <$ 631 kpc): $\Sigma_{\rm GC}(R) \propto R^{\alpha}$. Table 2 lists a summary of the fitting results. The radial profile of all GCs is fit well with the Sérsic parameters, $R_{\rm eff,1} = 28.5 \pm 3.2$ k pc and $n_1 = 0.1 \pm 0.1$ for the BCG component and $R_{\rm eff,2} = 224.5 \pm 22.1$ kpc, $n_2 = 1.3 \pm 0.3$ for the intracluster component. The outer region is also fit well with a power-law index $\alpha = -2.0 \pm 0.2$. The radial profiles of the blue and red GCs are also fit with similar

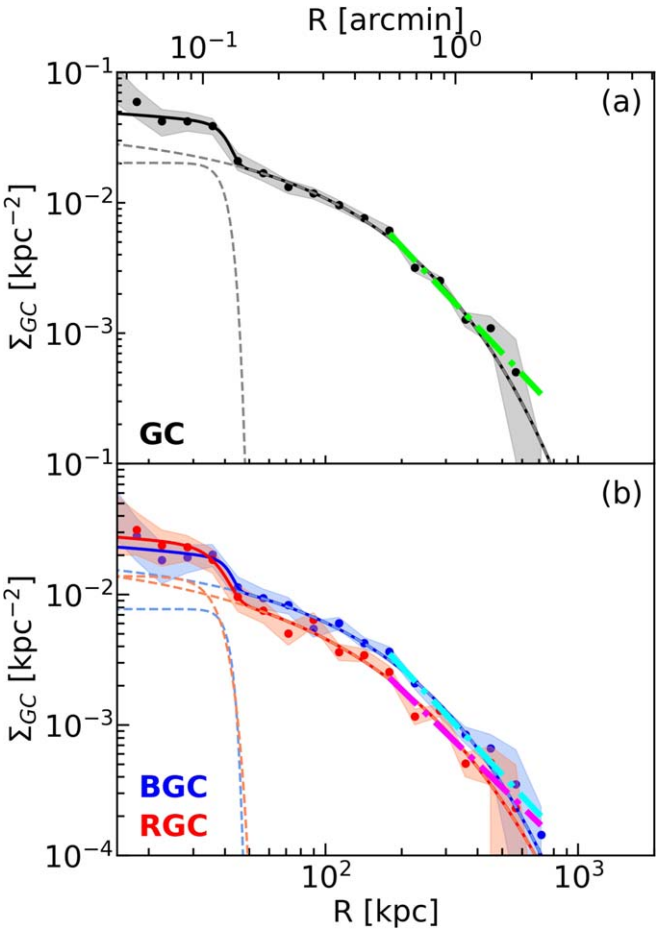

Figure 9. Radial number density profiles of the GCs (all GCs, black circles; blue GCs, blue circles; red GCs, red circles). Solid lines represent the two-component Sérsic-law fitting results for the central plus intracluster GC components (dashed lines for individual components). The black, blue, and red lines denote, respectively, fitting results for all, blue, and red GCs. Thick dotted–dashed lines denote the power-law fitting results for the outer region (158 kpc $< R <$ 631 kpc).

parameters: in the case of the blue GCs, $R_{\rm eff,1} = 29.3 \pm 7.0$ k pc, $n_1 = 0.1 \pm 0.2$ for the BCG component; $R_{\rm eff,2} = 238.9 \pm 29.1$ kpc, $n_2 = 1.3 \pm 0.3$ for the intracluster GC component; and $\alpha = -2.1 \pm 0.2$ for the outer region. In the case of the red GCs, $R_{\rm eff,1} = 26.7 \pm 3.4$k pc, $n_1 = 0.1 \pm 0.1$ for the BCG component; $R_{\rm eff,2} = 241.7 \pm 48.6$ kpc, $n_2 = 1.5 \pm 0.6$ for the intracluster GC component; and $\alpha = -1.9 \pm 0.3$ for the outer region.

Thus, the effective radius of the intracluster GC system is about eight times larger than that of the BCG GC system. The outermost region of the intracluster GC system is also represented

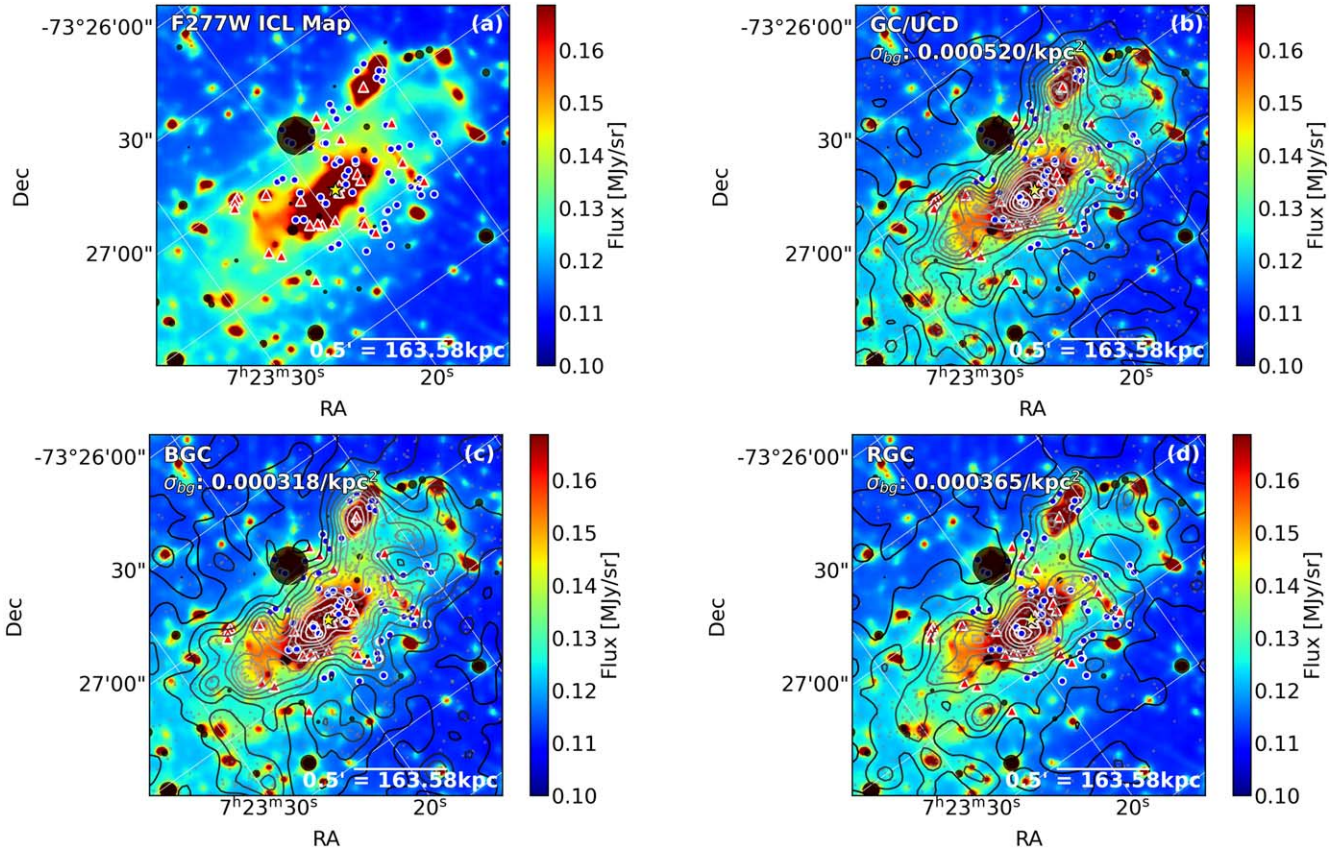

Figure 10. Comparison of the GC (all, blue, and red GCs) number density contour maps with the ICL map (pseudocolor map) of the F277W image of the central field that was derived from a median boxcar (51 × 51 pixels) smoothing filter. Red triangles and blue circles represent the known cluster member galaxies and the gravitational lens sources (Mahler et al. 2022), respectively. Black circles denote the bright stars with F200W$_0$ <22 mag, the sizes of which are scaled according to relative magnitudes. The yellow star is the center of the BCG. The color-scale bars represent the ICL surface brightness.

well by the power law with an index of $\alpha = -2.0 \pm 0.2$. This profile is slightly steeper than that of the intracluster GC system in the Virgo cluster, $\alpha = -1.5 \pm 0.1$ (Lee et al. 2010).

5. Discussion

5.1. Comparison with ICL Distribution

From the JWST/NIRCam images of SMACS 0723, Pascale et al. (2022) and Mahler et al. (2022) derived a smooth map of the diffuse light using a median boxcar filter with 21×21 and 100×100 pixels, respectively, showing the distribution of the ICL. They noted that the diffuse ICL is elongated along the major axis of the BCG but in a much more extended way. Also, they found two interesting substructures of the ICL: a large-scale loop in the west component of the BCG and a large lobe-like feature in the east component. To compare the distributions of the GCs and ICL, we similarly derive a smooth map of the diffuse light applying a median boxcar smoothing with 51×51 pixels to the F277W image and display it in Figure 10(a). We overlay the GC number density contour maps (all, blue, and red GCs) to the smooth map of the ICL in Figures 10(b)–(d). We also mark the positions of bright stars, known cluster member galaxies, and gravitational lens image sources (Mahler et al. 2022) in the figure.

Figure 10 shows several distinguishable features. First, the spatial distributions of the GCs and ICL are consistent in general. However, the GCs are found farther than the ICL boundary. Second, the western large-scale loop structure seen in the GC number density map is consistent with that of the ICL. A number of GCs are located along the loop of the diffuse ICL. Third, the GC number density map also shows an extended structure to the east of the BCG, which is consistent with the lobe-like diffuse component of the ICL. However, GC clump 1 (the strongest clump of GCs at $R \approx 200$ kpc east of the BCG) does not have a bright counterpart in the ICL map, although it is close to the boundary of the eastern loop. The GC clump 1 is better seen in the blue GC map, indicating that it is composed mainly of blue GCs.

5.2. Formation of SMACS 0723

The existence of a number of substructures with varying scales (in addition to the BCG) in the GC and ICL maps indicates that a large number of galaxy groups with diverse masses are falling to the cluster center, and they are in the middle of the merging process now. The elongated structure seen in the maps of the GCs and ICL indicates that most galaxies are falling to the cluster center along the east–west direction. These maps illustrate the distribution of the stars and GCs that are stripped off from their host galaxies or are the remnant of disrupted galaxies.

Considering the distributions of the GCs and ICL, G2 is probably a main host of a galaxy group that includes G3 (called the G2 group). Figure 10 shows that the G2 group and the BCG are connected not only in the GC map but also in the ICL map. The existence of the GCs and diffuse light between the G2 group and the BCG implies that both systems are physically

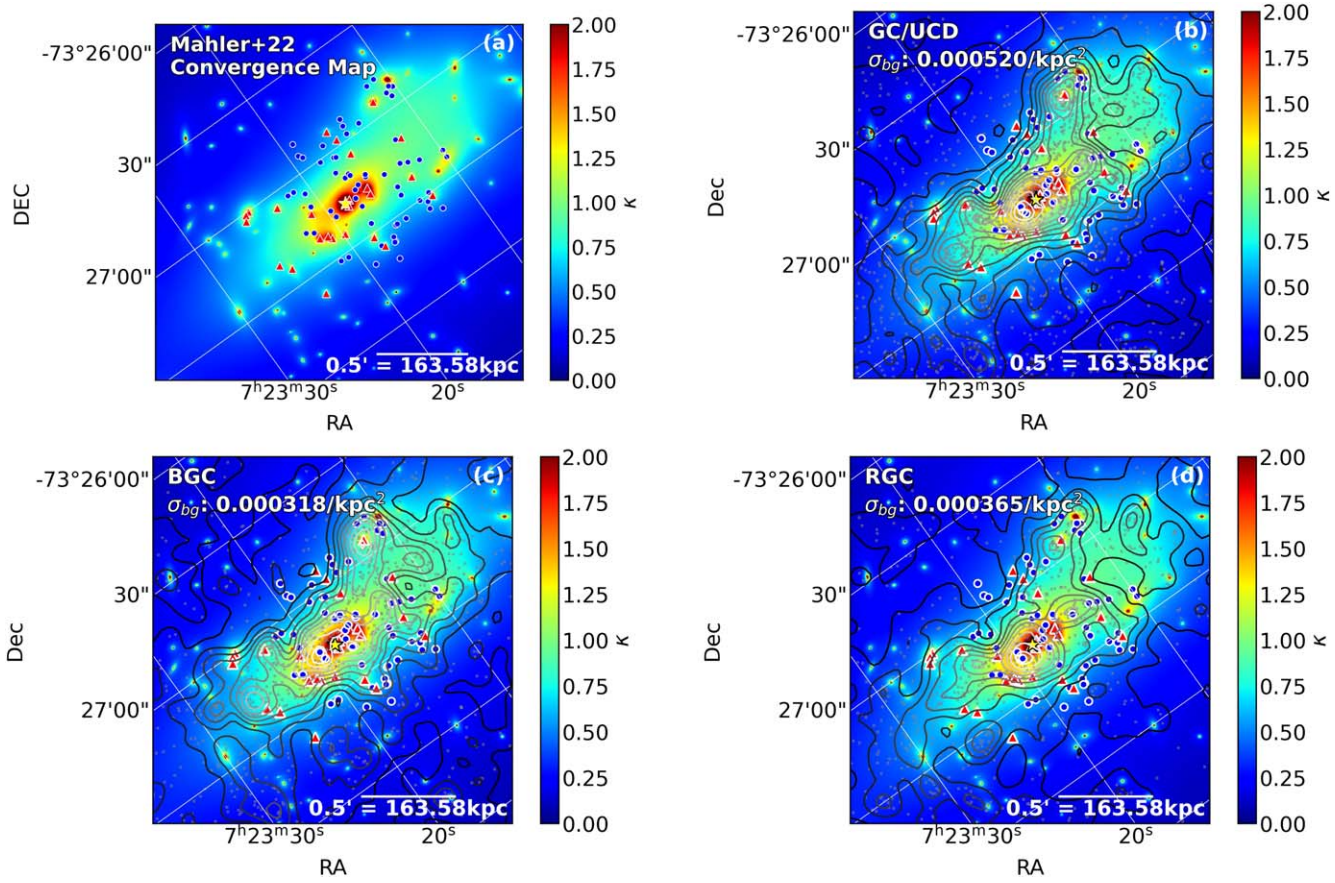

Figure 11. Comparison of the GC number density contour maps for the central field of SMACS 0723 with the dark matter surface mass density map (convergence map) from strong lensing models given by Mahler et al. (2022; pseudocolor map). Red triangles and blue circles represent the known cluster member galaxies and the gravitational lens sources (Mahler et al. 2022), respectively. The color-scale bars denote the convergence (the dark matter surface mass density normalized to the critical surface mass density).

interacting. This is similar to the case of the NGC 4839 group that is known to be falling to the Coma center, as shown in the observations of galaxies and various ICM, including the GCs (Briel et al. 1992; White et al. 1993; Colless & Dunn 1996; Lyskova et al. 2019; Churazov et al. 2021; Oh et al. 2022). The loop structure might have formed when the G2 group was falling to the cluster center, which needs to be investigated further in the future.

5.3. Comparison with X-Ray Brightness Distribution

A Chandra X-ray brightness map of SMACS 0723 is given in Mahler et al. (2022; their Figures 1 and 9). Comparing the GC number density map in this study with the X-ray map of SMACS 0723 given in Mahler et al. (2022), we find that both maps display generally similar structures in the sense that both show a large-scale elongated distribution. Interestingly, the X-ray contour map of the central region of SMACS 0723 (Figure 1 in Mahler et al. 2022) shows a distinguishable component at the position of the western loop structure in addition to the strongest peak at the BCG center. The location of this component is consistent with the center of the western loop in the GC number density and ICL maps.

5.4. Comparison with Dark Matter Distribution

Dark matter mass density maps (and radial profiles) of SMACS 0723 derived from the strong lensing analysis were presented by Caminha et al. (2022), Golubchik et al. (2022), Mahler et al. (2022), and Pascale et al. (2022), who used the JWST/NIRCam and HST/ACS/WFC3 images. In Figure 11, we overlay the GC number density contour maps on the dark matter surface mass density map (the convergence map, κ = surface mass density normalized to the critical mass density) provided by Mahler et al. (2022; pseudocolor maps). The GC and dark matter mass maps show remarkably similar structures in the sense that both show a large-scale structure that is elongated along the major axis of the BCG but much more extended than the BCG. They also show similar substructures.

Mahler et al. (2022) presented a comparison of the dark matter radial density profiles of SMACS 0723 they derived from the JWST/NIRCam images with those derived using different lensing models in the literature: RELICS-lenstool (Coe et al. 2019), RELICS-GLAFIC (Coe et al. 2019), and LTM (Golubchik et al. 2022; their Figure 6). In this comparison, the first three models produce similar profiles extending out to $R \approx 1$ Mpc, while the LTM profile is much more steeply declining in the outer region ($R \approx 500$ kpc).

In Figure 12, we present a comparison of the radial number density profiles of the GCs with the dark matter mass density profiles based on the lensing analysis (Mahler et al. 2022). This figure shows that the radial density profile of the GCs is very similar to those of the dark matter in the inner range of $R = 50$–200 kpc. However, it becomes steeper in the outer

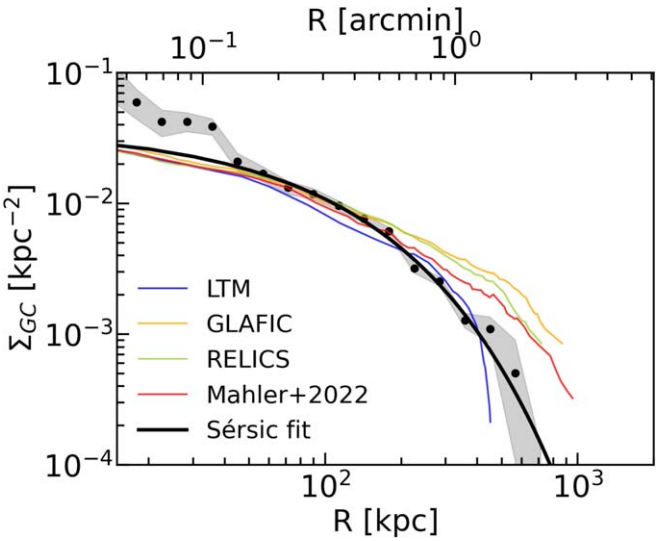

Figure 12. Comparison of radial number density profiles of the GCs in SMACS 0723 (black circles for the data and the thick black line for the fitting result of the intracluster component) and the dark matter mass density profiles from four strong lensing models given in Mahler et al. (2022; their Figure 6): RELICS-lenstool (Coe et al. 2019; light green line), RELICS-GLAFIC (Coe et al. 2019; yellow line), LTM (Golubchik et al. 2022; blue line), and Mahler et al. (2022; red line). The lensing model profiles were arbitrarily shifted to match the GC data for 50 kpc $< R <$ 200 kpc.

region at $R = 200$–600 kpc, deviating from the three lens models (RELICS-lenstool, RELICS-GLAFIC, and Mahler et al. 2022) and getting closer to the LTM model. However, the outermost GC profile is between the two model groups.

These results are consistent with those for the GCs found in the deep HST images of A2744, another massive cluster at $z = 0.308$ that is known as one of the most GC-abundant galaxy clusters (Lee & Jang 2016). Similar trends are also seen in the radial profiles of the intracluster GC number density and the dark matter mass derived from the simulated galaxy clusters selected from the cosmological simulations (Ramos-Almendares et al. 2018, 2020).

6. Summary

In the search of the GCs in the massive galaxy cluster SMACS 0723 using the early release JWST/NIRCam images, we find a large population of GCs that are spread over the cluster. These GCs are mostly intracluster GCs, as well as BCG GCs. The ages of these GCs, considering the cluster redshift, are younger than 9.5 Gyr. These GCs are about 8 Gyr old, if they formed as the Milky Way GCs.

The primary results are summarized as follows.

1. The F200W magnitudes of these GCs, 26.5 mag $<$ F200W$_0$ $<$ 29.5 mag, correspond to -15.2 mag $< M_{\rm F200W} < -12.2$ mag, showing that they belong to the brightest GCs (including the UCDs).
2. The spatial distributions of these GCs show a mega-parsec-scale structure that is elongated along the major axis of the BCG but much more extended than the stellar light of the BCG. In addition, they show a large number of substructures with various scales, some of which are consistent with the substructures in the map of the diffuse ICL.
3. The existence of the GCs and ICL between the G2 group and the BCG indicates that the G2 group is falling to the cluster center, as in the case of the NGC 4839 group in the Coma cluster. The large-scale loop structure to the west of the BCG might have formed when the G2 group was falling to the cluster center.
4. The GC number density map is, in general, consistent with the dark matter mass density map based on the strong lensing analysis in the literature in the sense that both show a large-scale elongated structure.
5. The radial number density profiles of the GCs are fit reasonably by the two-component Sérsic law: the BCG component and the intracluster GC component. The effective radius of the intracluster GC system is about eight times larger than that of the BCG GC system.
6. The radial number density profile of the GCs in the inner region at $R = 50$–200 kpc is very similar to the dark matter mass profile obtained from strong lensing models. However, it becomes steeper in the outer region at $R = 200$–600 kpc, deviating from the three lens models and getting closer to the LTM model. However, the outermost GC profile is between the two model groups.

All of these results, based on the excellent data obtained with the JWST/NIRCam, show that the intracluster GCs are an excellent independent tool to probe the dark matter distribution in galaxy clusters, as well as reveal the cluster assembly history. Object SMACS 0723 is only the first case of distant galaxy clusters showing the power of the JWST, and many more will come in the JWST era.

The authors are grateful to the anonymous referee for useful comments. This work was supported by the National Research Foundation grant funded by the Korean Government (NRF-2019R1A2C2084019). We thank Brian S. Cho for improving the English in the original manuscript. This work is based on observations made with the NASA/ESA/CSA James Webb Space Telescope. The data were obtained from the Mikulski Archive for Space Telescopes at the Space Telescope Science Institute, which is operated by the Association of Universities for Research in Astronomy, Inc., under NASA contract NAS 5-03127 for JWST.

Some/all of the data presented in this paper were obtained from the Mikulski Archive for Space Telescopes (MAST) at the Space Telescope Science Institute. The specific observations analyzed can be accessed via 10.17909/0txw-f070.

Facility: JWST.

Software: Numpy (Harris et al. 2020), Matplotlib (Hunter 2007), Scipy (Virtanen et al. 2020), Astropy (Astropy Collaboration et al. 2013, 2018), IRAF (Tody 1986), PyRAF (Science Software Branch at STScI 2012), Astroalign (Beroiz et al. 2020), DAOPHOT (Stetson 1987), SExtractor (Bertin & Arnouts 1996).

ORCID iDs

Myung Gyoon Lee https://orcid.org/0000-0003-2713-6744
Jang Ho Bae https://orcid.org/0000-0002-4477-1208
In Sung Jang https://orcid.org/0000-0002-2502-0070

References

Alamo-Martínez, K. A., & Blakeslee, J. P. 2017, ApJ, 849, 6
Alamo-Martínez, K. A., Blakeslee, J. P., Jee, M. J., et al. 2013, ApJ, 775, 20

Astropy Collaboration, Price-Whelan, A. M., Sipőcz, B. M., et al. 2018, AJ, 156, 123
Astropy Collaboration, Robitaille, T. P., Tollerud, E. J., et al. 2013, A&A, 558, A33
Beroiz, M., Cabral, J. B., & Sanchez, B. 2020, A&C, 32, 100384
Bertin, E., & Arnouts, S. 1996, A&AS, 117, 393
Boyer, M. L., Anderson, J., Gennaro, M., et al. 2022, RNAAS, 6, 191
Briel, U. G., Henry, J. P., & Boehringer, H. 1992, A&A, 259, L31
Caminha, G. B., Suyu, S. H., Mercurio, A., et al. 2022, A&A, 666, L9
Churazov, E., Khabibullin, I., Lyskova, N., et al. 2021, A&A, 651, A41
Colless, M., & Dunn, A. M. 1996, ApJ, 458, 435
Coe, D., Salmon, B., Bradač, M., et al. 2019, ApJ, 884, 85
Durrell, P. R., Côté, P., Peng, E. W., et al. 2014, ApJ, 794, 103
Faisst, A. L., Chary, R. R., Brammer, G., et al. 2022, arXiv:2208.05502
Fitzpatrick, E. L. 1999, PASP, 111, 63
Fox, C., Mahler, G., Sharon, K., et al. 2022, ApJ, 928, 87
Golubchik, M., Furtak, L. J., Meena, A. K., et al. 2022, ApJ, 938, 14
Graham, A. W., & Driver, S. P. 2005, PASA, 22, 118
Harris, W. E., Ciccone, S. M., Eadie, G. M., et al. 2017, ApJ, 835, 101
Harris, W. E., Brown, R. A., Durrell, P. R., et al. 2020, ApJ, 890, 105
Harris, W. E., Kavelaars, J. J., Hanes, D. A., et al. 2009, AJ, 137, 3314
Harris, C. R., Millman, K. J., van der Walt, S. J., et al. 2020, Natur, 585, 357
Hilker, M., Richtler, T., Barbosa, C. E., et al. 2018, A&A, 619, A70
Hunter, J. D. 2007, CSE, 9, 90
Indebetouw, R., Mathis, J. S., Babler, B. L., et al. 2005, ApJ, 619, 931
Iodice, E., Spavone, M., Cantiello, M., et al. 2017, ApJ, 851, 75
Jauzac, M., Richard, J., Jullo, E., et al. 2015, MNRAS, 452, 1437
Kang, J., & Lee, M. G. 2021, ApJ, 914, 20
Lee, M. G., Park, H. S., & Hwang, H. S. 2010, Sci, 328, 334
Lee, M. G., & Jang, I. S. 2016, ApJ, 831, 108
Lotz, J. M., Koekemoer, A., Coe, D., et al. 2017, ApJ, 837, 97
Lyskova, N., Churazov, E., Zhang, C., et al. 2019, MNRAS, 485, 2922
Madrid, J. P., O'Neill, C. R., Gagliano, A. T., et al. 2018, ApJ, 867, 144
Mahler, G., Jauzac, M., Richard, J., et al. 2022, arXiv:2207.07101
Montes, M., & Trujillo, I. 2022, arXiv:2209.00043
Mowla, L. A., Iyer, K. G., Desprez, G., et al. 2022, ApJL, 937, L35
Oh, S., Lee, M. G., & Jang, I. S. 2022, ApJ, in press
Oliveira, R. A. P., Souza, S. O., Kerber, L. O., et al. 2020, ApJ, 891, 37
Pascale, M., Frye, B. L., Diego, J., et al. 2022, arXiv:2207.07102
Peng, E. W., Ferguson, H. C., Goudfrooij, P., et al. 2011, ApJ, 730, 23
Pontoppidan, K., Blome, C., Braun, H., et al. 2022, ApJL, 936, L14
Ramos-Almendares, F., Abadi, M., Muriel, H., et al. 2018, ApJ, 853, 91
Ramos-Almendares, F., Sales, L. V., Abadi, M. G., et al. 2020, MNRAS, 493, 5357
Repp, A., & Ebeling, H. 2018, MNRAS, 479, 844
Rigby, J., Perrin, M., McElwain, M., et al. 2022, arXiv:2207.05632
Rodrigo, C., & Solano, E. 2020, in XIV.0 Scientific Meeting (virtual) of the Spanish Astronomical Society, 182 https://www.sea-astronomia.es/reunion-cientifica-2020
Rodrigo, C., Solano, E., & Bayo, A. 2012, IVOA Working Draft 15 October, 2012 doi:10.5479/ADS/bib/2012ivoa.rept.1015R
Schlafly, E. F., & Finkbeiner, D. P. 2011, ApJ, 737, 103
Schlegel, D. J., Finkbeiner, D. P., & Davis, M. 1998, ApJ, 500, 525
Science Software Branch at STScI 2012, ascl soft, ascl:1207.011
Sérsic, J. L. 1963, BAAA, 6, 41
Stetson, P. B. 1987, PASP, 99, 191
Tody, D. 1986, Proc. SPIE, 627, 733
Virtanen, P., Gommers, R., Oliphant, T. E., et al. 2020, Nat. Methods, 17, 261
White, S. D. M., Briel, U. G., & Henry, J. P. 1993, MNRAS, 261, L8